Article

# Trajectory of the Selective Dissolution of Charged Single-Walled Carbon Nanotubes

David J. Buckley,[†] Stephen A. Hodge,[‡] Martina De Marco,[‡] Sheng Hu,[‡] David B. Anthony,[‡] Patrick L. Cullen,[†] Kevin McKeigue,[§] Neal T. Skipper,[†] Milo S. P. Shaffer,[‡] and Christopher A. Howard*,[†]

[†]Department of Physics and Astronomy, University College London, Gower Street, London WC1E 6BT, United Kingdom.
[‡]Department of Chemistry, Imperial College London, South Kensington Campus, London SW7 2AZ, United Kingdom
[§]Linde LLC, Murry Hill, New Jersey 07974, United States

**S** *Supporting Information*

**ABSTRACT:** Single-walled carbon nanotubes (SWCNTs) are typically produced as a mixture of different lengths and electronic types. Methods for sorting these as-produced mixtures typically require damaging and unscalable techniques to first overcome the strong bundling forces between the nanotubes. Previously, it has been shown that negatively charging SWCNTs can lead to their thermodynamically driven, gentle dissolution in polar solvents, and moreover that this process can selectively dissolve different SWCNT species. However, there are several conflicting claims of selectivity that must be resolved before the full potential of this method for scalably postprocessing SWCNTs can be realized. Here we carefully investigate dissolution as a function of charge added to the as-produced SWCNT sample, using a range of complementary techniques. We uncover a far richer dependence on charge of SWCNT dissolution than previously imagined. At low values of charge added, amorphous carbons preferentially dissolve, followed sequentially by metallic, larger diameter (>9 Å) semiconducting SWCNTs, and finally smaller diameter semiconducting SWCNTs as more charge is added. At an optimal stoichiometry of $NaC_{10}$, the dissolution yield is maximized across all species. However, at higher charge the larger diameter and metallic SWCNTs are so highly charged that they are no longer soluble, leaving smaller diameter SWCNTs in solution. Our results clearly demonstrate two interconnected mechanisms for dissolution: the sequential charging of the SWCNTs and their solution thermodynamics. This work reconciles conflicting reports in the literature, demonstrates that upon charge added the different SWCNTs behave like discrete molecular species, and points toward selective dissolution as a scalable method for SWCNT separation.
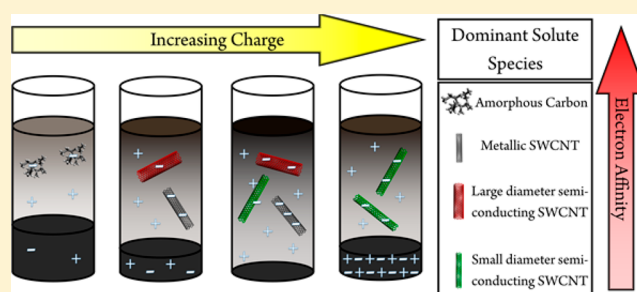
## 1. INTRODUCTION

Despite advances in selective synthesis,[1−3] as-grown single-walled carbon nanotube (SWCNT) samples typically consist of a mixture of lengths (0.1 μm–several μm), diameters (0.4–5 nm), and electronic types (approximately 1:2 metallic, m-SWCNTs to semiconducting sc-SWCNTs),[4] tightly held together in bundles which are decorated in residual metal catalyst and amorphous carbon.[5] Many "postsynthesis" methods that aim to refine this mix into homogeneous samples have been explored. However, most of these methods rely on processes that are detrimental to the pristine properties of the SWCNTs and/or are difficult to scale. For example, initial purification steps, necessary to remove carbonaceous materials or catalyst particles, are often performed with nitric acid refluxing[5] or acid/base mixtures,[6] which can damage the atomic framework of the SWCNT.[7] Furthermore, a prerequisite for most enrichment procedures is the individualization of SWCNTs from their bundles. Dispersions are typically achieved by energetic processes such as ultrasonication to separate the SWCNTs from one another and then ultracentrifugation to

separate the unbundled fraction.[8,9] The sonication damages and shortens the nanotubes,[10] while the (sometimes multiple) ultracentrifugation step is difficult to scale.[11]

An alternative to shear-based processing is reductive chemistry, a versatile route for the efficient solubilization of a range of important nanomaterials.[12−15] When applied to SWCNTs, reductive processing (i.e., controllably adding electrons to the nanomaterials) can lead to spontaneous, gentle dissolution of individualized SWCNTs in polar aprotic solvents, avoiding the damage associated with other methods.[12,13,16,17] The reduced SWCNTs can be generated either chemically (with sodium naphthalide,[12] alkali metal,[18] or alkali metal–ammonia[13] to form so-called nanotubide salts) or electrochemically.[16] The dissolution is spontaneous so requires no damaging energy input or centrifugation, and the process is intrinsically scalable. Moreover, there are several reports that

specific SWCNTs dissolve preferentially; i.e., reductive dissolution can be used for scalable postsynthesis separation of SWCNTs. Unfortunately, there are clear inconsistencies between the reported enrichments. SWCNTs charged in alkali metal−ammonia and subsequently dissolved in *N,N*-dimethyl-formamide (DMF) manifested only a selective dissolution of the m-SWCNTs.[13,18] However, in one case this result is contradicted by the same apparent separation observed in the undissolved material.[18] Another study on metal−ammonia reduced SWCNTs reported the preferential *chemical function-alization* of both m-SWCNTs and smaller diameter sc-SWCNTs upon charging.[19] In contrast, another study showed that sodium naphthalide reduced nanotubide salts could lead to the preferential dissolution of larger diameter nanotubes of both types.[20] Electrochemically reduced SWCNTs samples showed a preferential dissolution of amorphous carbon, but not of the different nanotube species.[16] Potential sources of these discrepancies are the reliance on Raman spectroscopy to assess separation,[13,17,18,20] the physical agitation often used to encourage the dispersion of the SWCNTs,[18] a range of charging stoichiometries used, and the dependence of the process on the exact composition of the as-synthesized SWCNT starting material which can vary with the production method and batch. Raman spectroscopy can be misleading, as it examines a small sample of SWCNT types for each laser excitation, it is highly sensitive to the environment, and the effect of diameter and metal/semiconductor enrichment are often indiscriminable.[21,22] Bundling can narrow and shift the resonant energies of the SWCNTs, causing peak intensity and position shifts and making full population analysis prohibitively difficult. Furthermore, functionalization can mask the unique SWCNT electronic structure, and selectivity induced by sample heating/damage from laser irradiation can affect both the radial breathing mode (RBM) signals and the intensity ratio between the sp$^2$-associated G-mode and the defect-induced D-mode ($I_{G+}/I_D$ ratio).[23−27] It is also important to note that dispersions obtained via stirring or sonication will impede assessment of the truly selectively *dissolved* fraction.

To develop a full understanding of the selective dissolution of reduced SWCNTs, a multitechnique analysis of the spontaneously dissolved fraction as a function of charge added to SWCNT was performed. In this way, it can be unambiguously demonstrated that the selective dissolution is highly dependent on charging stoichiometry. Furthermore, these results highlight the two competing dissolution mechanisms: (i) selective charging based on the relative electron affinities of the different SWCNTs and (ii) the thermodynamic instability of the solutions at high charge densities.

Nanotubide salts with carefully controlled charge/carbon ratios were prepared via reducing SWCNT samples with solvated electrons generated by dissolving alkali metals in liquid ammonia (methods, Scheme 1). In brief, the SWCNTs and a stoichiometric amount of sodium are loaded into a vessel into which anhydrous ammonia was condensed. The ammonia was then evaporated to leave a nanotubide salt. These salts were subsequently dissolved in DMF in an argon glovebox for 3 days, without any stirring or physical agitation. Nanotubide salts were prepared with the stoichiometry $NaC_x$ (where $x$ = 200, 150, 100, 40, 20, 10, 5). These ratios give a charge density (electrons per carbon atom) of 0.005, 0.0067. 0.01, 0.025, 0.05, 0.1, and 0.2, respectively. For clarity, dissolved SWCNT fractions from each salt will be referred to as $(NaC_x)_{DIS}$ and

**Scheme 1. Formation of SWCNT Nanotubide, $NaC_x$, Following Reductive Treatment with Solvated Electrons from Sodium−Ammonia Solutions, Followed by Dissolution in a Dry Polar Aprotic Solvent (DMF)**



i. Na/NH$_3$, 223 K, 12 hours

ii. DMF, RT, 3 days
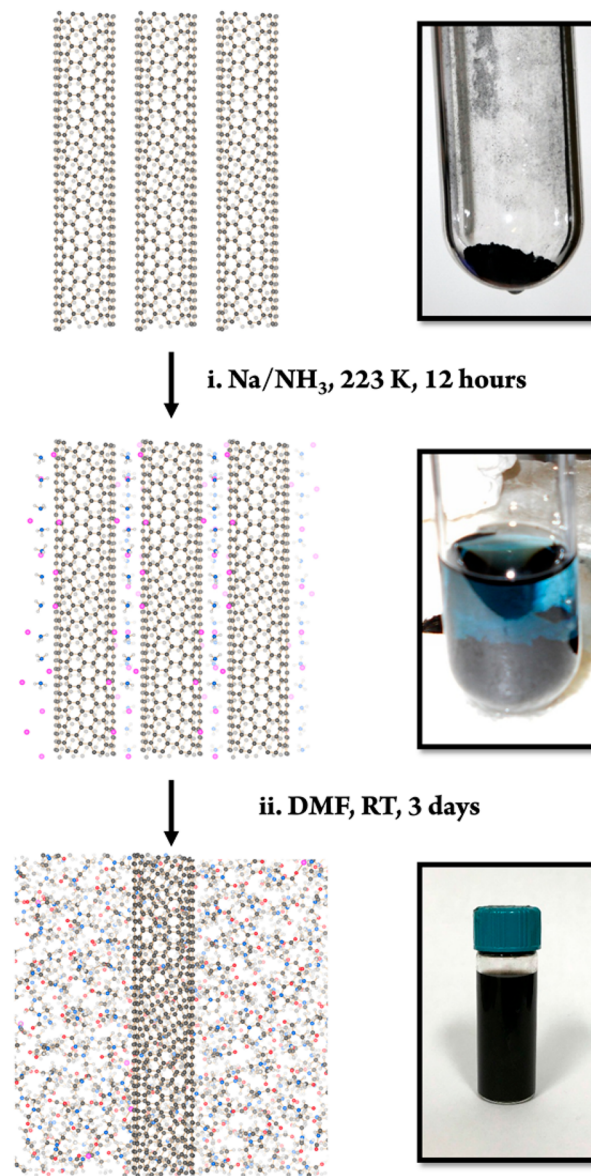
undissolved fractions as $(NaC_x)_{UND}$, where $NaC_x$ is the stoichiometry of the nanotubide salt after ammoniation.

## 2. EXPERIMENTAL DETAILS

**2.1. Chemicals.** HiPco SWCNTs Batch R2-172 and Batch R1-821 were from NanoIntegris Technologies Inc. *N,N*-Dimethylformamide (DMF, ≥ 99.8%), sodium ingot (≥99.95%), anhydrous ammonia (NH$_3$ ≥ 99.95%), nitric acid (HNO$_3$, 70%), hydrochloric acid (HCl, 37%), sodium deoxycholate (DOC, ≥ 97%), and deuterium oxide (D$_2$O, 99.9 atom %) were all from Sigma-Aldrich Co and used as supplied unless otherwise stated.

**2.2. Ammonia Condensation.** *2.2.1. SWCNT Prepara-tion.* As-received HiPco SWCNTs were dried in a vacuum oven at 80 °C to remove residual ethanol before being vacuum annealed at 500 °C under a turbo-vacuum to at least $1 \times 10^{-6}$ mbar for a minimum of 12 h to remove oxygen and moisture.

The SWCNTs were taken to the argon glovebox with no further atmospheric exposure.

*2.2.2. Nanotubide Production.* The SWCNTs were added to a quartz reaction tube with the stoichiometric amount of sodium ingot and sealed at the valve before being removed from the glovebox. The reaction tube was immersed in an isopropyl alcohol bath at −50 °C and attached to the ammonia rig, which was evacuated with a turbopump to $1 \times 10^{-6}$ mbar before the tube was opened to the vacuum. The ammonia was then expanded into a known buffer volume (300 cc) on the rig and the pressure recorded, followed by the condensation onto the sample. This expansion step was repeated until 15 bar liters was condensed. A blue color was observed showing the solvation of the electron (and the sodium cation), before the ammonia lost color due to the reduction of the SWCNTs. This condensation was left for 12 h before the ammonia lecture bottle was cooled using liquid nitrogen and the ammonia was cryopumped back from the reaction tube. When all the ammonia had evaporated from the sample, the reaction tube was sealed and taken back into the glovebox. In a typical experiment, ~100 mg of nanotubide (mass corrected to subtract the mass due to sodium) was spontaneously dissolved in 100 mL of anhydrous DMF with no stirring or sonication. After 3 days, the concentrations remained constant, and these supernatants were investigated for chiral distributions.

**2.3. Yield Measurements.** *2.3.1. TGA-Mass Spectrometer.* An aliquot, 80 μL, of the supernatants was decanted into alumina crucibles and inserted into a Mettler Toledo TGA/DSC 1LF/UMX with an attached HIDEN HPR20-QIC EGA mass spectrometer. The samples were held at 200 °C in air until no DMF signature ($M = 73$ g mol$^{-1}$) was detected from the evolved gas. The sample was then heated to 600 °C in air at 10 °C min$^{-1}$ to degrade the carbon and leave residual metal oxides and hydroxides from the iron catalyst and sodium.

*2.3.2. Mass Filtration.* A portion, 5 mL, of the supernatant was mixed with 250 mL of DMF in a Büchner funnel and vacuum filtrated on top of a 0.2 μm pore size poly(tetrafluoroethylene) (PTFE) filter paper. The SWCNT film produced on the paper was washed with 250 mL each of ethanol (99.8%), chloroform (≥99%), and deionized water (18 MΩ) before drying in the oven at 80 °C to remove residual water. A balance with an accuracy of ±5 μg was used to measure the mass of the PTFE filter paper before and after filtration, under ambient conditions.

*2.3.3. UV−Vis−NIR Absorption.* To measure concentration, the supernatants were decanted into a 10 mm path length, sealed quartz cuvette and the lid was further wrapped in Parafilm. Scans were performed on a PerkinElmer Lambda 950. If the absorbance exceeded 3 AU, samples were diluted 10 times using DMF and repeated.

**2.4. Chiral Analysis.** *2.4.1. Raman Spectroscopy.* Drops of 1 mL of nanotubide solutions were deposited onto glass microscope slides and allowed to dry in an argon glovebox atmosphere. Raman spectroscopy was performed on each dissolved fraction. Spectra were collected on a Renishaw inVia micro-Raman spectrometer with 532 nm (2.33 eV) DPSS diode (numerical aperture 0.8/100×, sample power 3.2 mW, WiRE 4.1 HF7241 software 2014 interface, Renishaw PLC, U.K.) in backscattered geometry, with laser spot diameters 0.8 μm. Raman spectra were processed and Raman maps produced using WiRE software (using spectra that were background corrected and normalized to the G$^+$-mode unless otherwise

stated). For each sample, a 400 μm$^2$ map was recorded on a point by point basis, with each spectrum on a 1 μm$^2$ region.

*2.4.2. Aqueous Dispersions of SWCNTS for PL Spectroscopy and UV/Vis/NIR Absorption.* The supernatants were dried in an evaporation dish in the argon glovebox on a hot plate at 160 °C, and the SWCNTs were recovered. The SWCNT solute was then placed into a reaction tube and outgassed at 500 °C for 24 h under a static vacuum of $1 \times 10^{-6}$ mbar to sublime the sodium metal. The sublimed sodium condensed as a mirror at the cold end of the reaction tube. The SWCNTs were then exposed to atmosphere and 15 mg mixed with 30 mL of a solution of 1 wt/vol % DOC/D$_2$O. The mixture was placed in an isopropyl alcohol bath at 0 °C and ultrasonicated for $2 \times 15$ min using a Sonics & Materials VCX750-220 V tip probe (225 W). The resultant dispersions were ultracentrifuged with a Beckmann Coulter Optima L-90K with SW41Ti swinging bucket rotor at 120 000 g for 40 min, and only the top 50% of the supernatants were recovered.

*2.4.3. PL Spectroscopy.* The nanotube dispersions were investigated using an Applied Nanofluorescence NS1 Nanospectralyzer. A cuvette with a 4 mm path length was filled with 2 mL of SWCNT dispersion was scanned with a 500 ms integration time on 3 lasers (638, 691, and 782 nm). Scans were averaged over 30 measurements, and emission was detected with an InGaAs detector cooled to −18 °C. Fitting was performed by the software supplied with the NS1, and abundances were calculated from predetermined optical absorption cross sections.

*2.4.4. UV−Vis−NIR.* Background scans used the 1 wt/vol % DOC/D$_2$O solution. The dispersions used were the same as for the PL spectra and performed on a PerkinElmer Lambda 950.

**2.5. Additional Characterization Techniques.** *2.5.1. ICP-AES.* Supernatants of nanotubide solutions were dried in evaporation dishes at ambient temperature in the glovebox before exposure to the atmosphere. The powders were then thermally degraded via TGA using the same methodology as the yield measurement, to obtain the carbon mass. The residue was dissolved in aqua regia (3 parts 37% hydrochloric acid to 1 part 72% nitric acid), and ICP-AES was performed on a PerkinElmer ICP 2000 DV OES.

*2.5.2. Electron Microscopy.* Imaged SWCNT samples were recovered after vacuum annealing (500 °C, $1 \times 10^{-6}$ mbar). The SWCNT powders were adhered using silver paint (Acheson silver DAG 1415 M) to Al stubs with all preparatory supplies purchased from Agar Scientific, U.K. Field emission gun SEM (Leo Gemini 1525 with SmartSEM software interface V05.05.03.00, 2010, Carl Zeiss NTS Ltd., U.K.) was operated in secondary electron detection mode at 5 keV at a working distance of approximately 10 mm.

## 3. RESULTS AND DISCUSSIONS

**3.1. Yield of Dissolution.** The percentages of the nanotubide salts that spontaneously dissolved in the DMF (Figure 1) were obtained via three methods: ultraviolet−visible−near-infrared (UV−vis−NIR) absorption, membrane filtration of the solute, and thermogravimetric analysis (TGA) of the nanotubide solutions. The most suitable method to evaluate the yield of dissolution was determined to be membrane filtration, since it measures the entirety of the SWCNT sample (nanotubes, catalyst particles, and amorphous carbon, but no sodium). TGA leaves the iron oxide residue from the catalyst and sodium (hydr)oxide used in the charging process and therefore underestimates the yield,[28] and
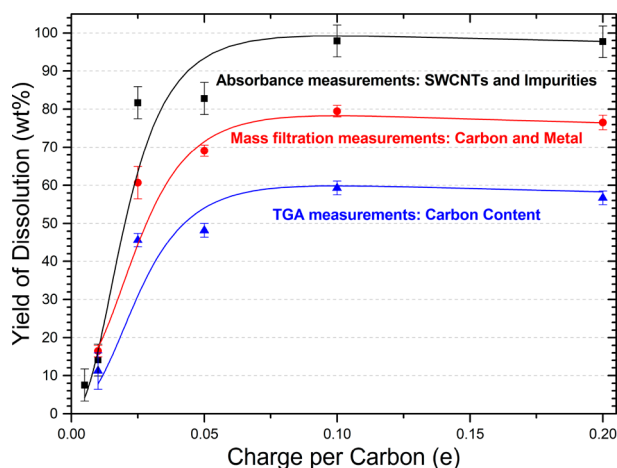
**Figure 1.** Nanotubide salt dissolution yields in the solvent DMF, as a function of charge added to the as-produced powder for different characterization techniques. Black squares represent measurements based on the absorbance at 660 nm. Red circles represent the mass measurements via membrane filtration. Blue triangles represent mass measurements from TGA after oxidative decomposition. The solid lines shown are a guide to the eye.

absorbance measurements introduce issues of extra light scattering due to doping, causing an overestimation[29] (a revised value for the extinction coefficients can be found in Figure S1). The maximum yield of dissolution obtained was ~80 wt % from a salt of stoichiometry of $NaC_{10}$. Notably, this yield is much higher than previous reports for a purely spontaneous dissolution[13,30] (i.e., with no sonication or stirring). With low charge added (between 0.005 and 0.01 $e/C$, $NaC_{200-100}$) the yield of dissolution is low (<18 wt %). As the amount of charge added increases, so too does the concentration of solution, with a maximum of 79.5 wt % occurring at $NaC_{10}$ (0.1 $e/C$). Interestingly, higher charging results in a decreased yield of 76 wt %. Although relatively small, this decrease is observed in all three methods, indicating that it is a real effect. To investigate the extent to which the dependence of the yield of dissolution on charge added is due to the preferential dissolution of different species, Raman, UV–vis–NIR absorption, and photoluminescence (PL) spectroscopies were utilized.

**3.2. Raman Spectroscopy: sp² Purity.** Raman spectroscopy can be used to probe the proportion of defective material in a SWCNT sample, by evaluating the intensity ratio of the structural order/disorder modes $I_{G+}/I_D$,[31] and also to determine the relative population of the different SWCNT types via analysis of the RBMs.[32] Here, this technique was used to assess the defectiveness of the dissolved species and as a qualitative guide for selectivity, the latter requiring corroboration with the other spectroscopic techniques used in this work, as Raman spectroscopy by itself can be misleading. Measurements were taken from the spontaneously dissolved SWCNTs from each salt, dried onto substrates and exposed to dry air to oxidize the reduced SWCNTs.[33−35]

The dissolved SWCNTs from the lowcharge stoichiometry salt $(NaC_{100})_{DIS}$ give the lowest $I_{G+}/I_D$ ratio, indicative of the highest amount of amorphous carbon and/or defective material (Figure 2b, c). As the concentration of sodium in the salt increases, the $I_{G+}/I_D$ ratio of the dissolved fraction monotonically increases, with the highest ratio from $(NaC_5)_{DIS}$. To better
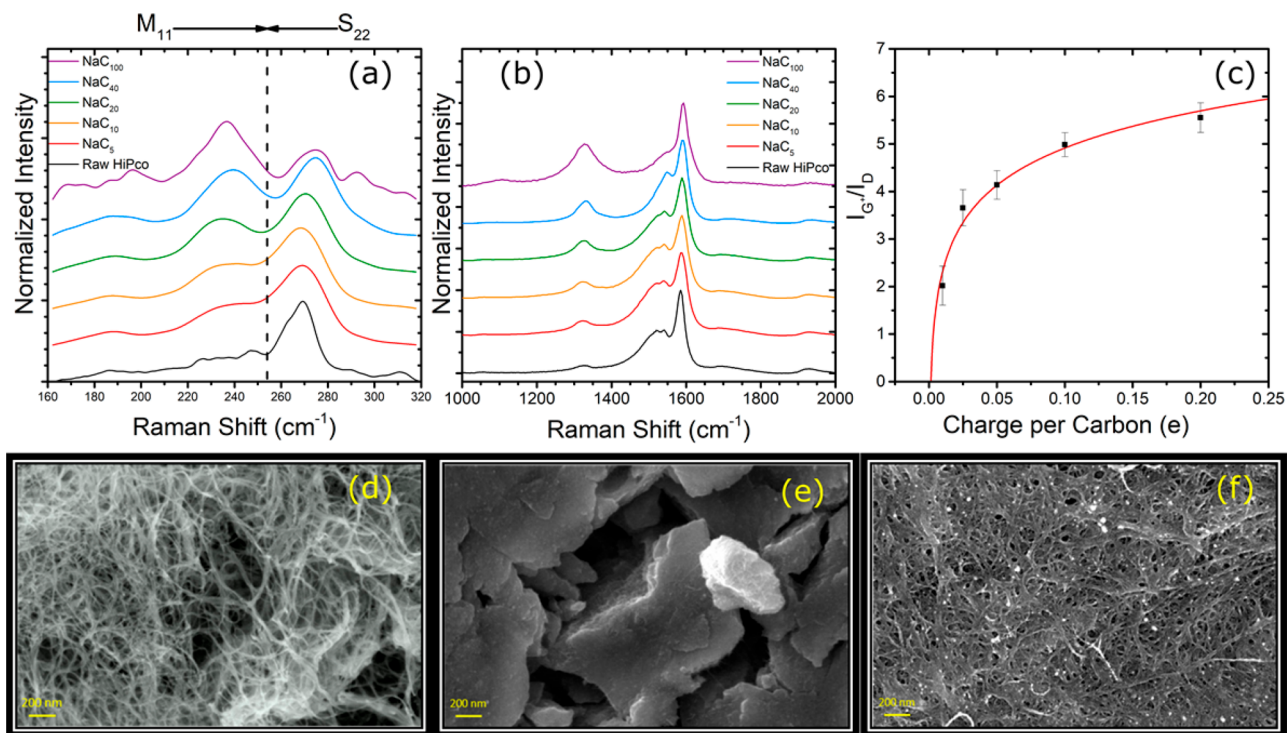


**Figure 2.** (a) Dissolved fraction Raman spectra with varying charge stoichiometry using a 532 nm laser, showing the RBM region (100−350 cm$^{-1}$), normalized to the largest feature. (b) The D-mode disorder peak (~1350 cm$^{-1}$) and G-mode graphitic peaks (~1510−1580 cm$^{-1}$) for each dissolved fraction, normalized to the intensity of the G$^+$-mode. (c) The $I_{G+}/I_D$ ratio as a function of charge stoichiometry showing increasing purity with increasing charging. (d) SEM of the starting HiPco SWCNT material. (e) SEM of the dissolved $(NaC_{100})_{DIS}$ nanotubide, with few visible SWCNT bundles. (f) SEM of the undissolved $(NaC_{100})_{UND}$ nanotubide showing the change in morphology from the starting material.

understand the origin of the decreased $I_{G+}/I_D$ ratio, scanning electron microscopy (SEM) was performed on the undissolved and dissolved fractions of the $NaC_{100}$ salt (Figure 2d–f). The dissolved fraction (Figure 2e) consists mostly of nontubular material, with very few visible nanotube bundles present. Contrastingly, the undissolved fraction (Figure 2f) is comprised of nanotube bundles albeit with a denser morphology than the starting material (Figure 2d) and an improved $sp^2$ structural quality from the corresponding Raman $I_{G+}/I_D$ ratio (Figure S2). This indicates that amorphous carbon, rather than defective SWCNTs, preferentially dissolves in the lowest charging regime.[36]

Concerning the selective dissolution of SWCNTs, a clear reduction is observed in the relative intensity of the peak at $\sim 268$ cm$^{-1}$, (attributed to the RBM of the (7,6) sc-SWCNT)[37] relative to the peak at 233 cm$^{-1}$ (attributed to the RBM of the (9,6) m-SWCNT) upon increasing charge (Figure 2a). The change indicates an enrichment of m-SWCNTs, in agreement with previous reports.[13,18] However, this decrease is also consistent with the conclusion that the larger diameter SWCNTs dissolve first, in agreement with other studies.[20] The multicomponent G$^-$-mode at $\sim 1510$–1550 cm$^{-1}$ in Figure 2b is also dependent on SWCNT type in the excited (resonant) population. The decreasing intensity of the mode at $\sim 1522$ cm$^{-1}$ relative to the $\sim 1545$ cm$^{-1}$ mode at lower charging again indicates that the dissolved SWCNTs are larger in diameter and the overall diameter distribution is narrower.[38] Furthermore, the broadening and asymmetry of the G$^-$-mode can also be attributed to a relative increase in the population of metallic species.[39,40]

**3.3. UV–vis–NIR Spectroscopy: m-SWCNT Enrichment.** PL and UV–vis–NIR absorption can be used to quantitatively analyze the $(n, m)$ enrichment of a SWCNT sample, being less sensitive to environmental effects than resonant Raman spectroscopy (although PL only probes sc-SWCNTs[41]). For both techniques it was necessary to first separate, decharge, dry, and redisperse the spontaneously dissolved fraction in water using standard protocols (see methods).[42] The decharging is required because the optical transitions of individual SWCNTs depend on their electronic structure, which will change upon charge doping.[29,43] Different species of isolated SWCNTs absorb light in the UV–vis–NIR regime at different characteristic energies based on their band structure, enabling an analysis of populations of different SWCNTs in a mixed as-produced sample. However, the absorption peaks obtained can be broad and overlapping, complicating the analysis. This challenge is compounded by the difficulty in deconvoluting the wavelength-dependent background, usually performed with a fitted $\lambda^{-a}$ (where $\lambda$ is the wavelength and $a$ is the fitted variable) or an exponential line shape.[44,45] However, toward higher wavenumbers (>20 000 cm$^{-1}$) the background has an extra contribution from a $\pi$-band surface plasmonic excitation present in all carbon $sp^2$ materials. In addition there is extra scattering intrinsic to the presence of m-SWCNTs, scattering from amorphous carbon, catalytic impurities, damaged and/or functionalized SWCNTs from the ultrasonication process, and bundled SWCNTs. As a result, the fitting of a single function across the entire sample becomes prohibitive. In this work, these factors are addressed by use of an ISO standard[46] of linear background subtraction, as is further discussed in the Supporting Information.

At the lowest salt charge stoichiometries $(NaC_{200-150})_{DIS}$, no features were observed in the UV–vis–NIR spectra, consistent

with the dissolution of only amorphous and defective material. For all other stoichiometries, the resultant spectra showed characteristic SWCNT absorption transitions (Figure 3). The
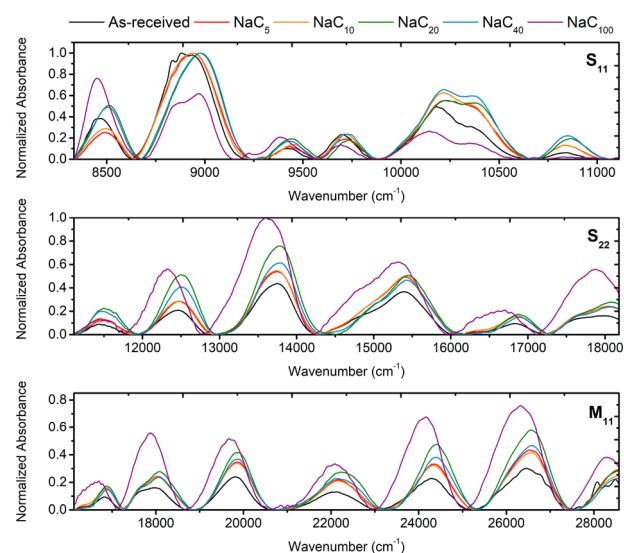


**Figure 3.** UV–vis–NIR spectra with varying $NaC_x$ ratios showing preferential dissolution of metallic SWNTs at low charge stoichiometries. Top: semiconducting SWCNT $S_{11}$ transitions. Middle: sc-SWCNT $S_{22}$ transitions. Bottom: m-SWCNT $M_{11}$ transitions. All spectra shown are baseline corrected and normalized to the largest peak intensity. The $NaC_{100}$ shows the biggest change, with a decrease for peaks in the $S_{11}$ region and increase in the $M_{11}$ region, showing metallic enrichment for this charge ratio.

percentage ratios of m-/sc-SWCNTs in the dissolved fractions were calculated by the ratio of the areas of the $M_{11}$ and $S_{11}$ transitions (Table 1).[46–48] The as-produced material was found

**Table 1. Change in Ratio of m-SWCNT/sc-SWCNT with Changing Charge Stoichiometry of the Dissolved Fractions from the UV–Vis–NIR Analysis**

| sample | % m-SWCNT ± 0.5 | % sc-SWCNT ± 0.5 |
|---|---|---|
| HiPco R2–172 | 26.2 | 73.8 |
| $NaC_5$ dissolved | 32.5 | 67.5 |
| $NaC_{10}$ dissolved | 31.2 | 68.8 |
| $NaC_{20}$ dissolved | 34.8 | 65.2 |
| $NaC_{40}$ dissolved | 30.3 | 69.7 |
| $NaC_{100}$ dissolved | 55.9 | 44.1 |
| $NaC_{150}$ dissolved | n/a | n/a |
| $NaC_{200}$ dissolved | n/a | n/a |

to have a metallic fraction of 26.2%, in good agreement with previous literature values.[49] For $(NaC_{100})_{DIS}$, a dramatic increase in the m-SWCNT fraction is found, more than doubling to 55.9%. However, at higher charging $(NaC_{40-5})_{DIS}$, the metallic enrichment is indiscernible, with a third of the sample now being made up of m-SWCNTs.

To investigate the enrichment for the $(NaC_{100})_{DIS}$ sample in more detail, the relative percentage changes of individual SWCNT $(n, m)$ populations (indexed from empirical data from UV–vis–NIR[50]), with respect to the raw sample, were calculated (Figure 4). The m-SWCNTs all show enrichment in the dissolved fraction as expected, though a slight preferential dissolution of the larger diameter m-SWCNTs can be observed.
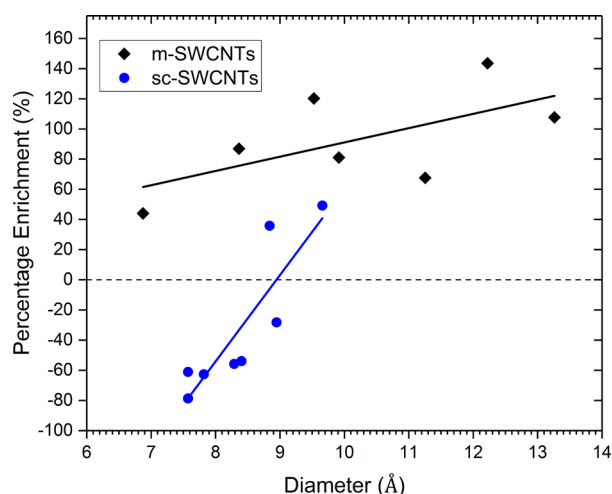
**Figure 4.** UV−vis−NIR relative percentage change of the $(NaC_{100})_{DIS}$ dissolved fractions relative to the starting material of assigned m-SWCNTs (black) and sc-SWCNTs, (red) showing the preferential dissolution of larger diameter SWCNTs. The solid lines are linear fits of the data as a guide to the eye.

For sc-SWCNTs, there is a dramatic diameter effect: the fraction of larger diameter sc-SWCNTs increases, whereas the fraction of smaller sc-SWCNTs decreases. The same analysis was performed on the undissolved fraction, $(NaC_{100})_{UND}$, since previous studies have had issues with observation of the same enrichment on both fractions.[18] Crucially, here we found the

complementary trend, that is, a decrease in larger diameter population in the $(NaC_{100})_{UND}$ material (Figure S4) confirming a genuine enrichment. For sc-SWCNTs, it is possible to quantify the $(n, m)$ population changes with greater accuracy using PL spectroscopy.

**3.4. Photoluminescence Spectroscopy: sc-SWCNT Diameter Enrichment.** PL spectroscopy was performed for all samples, and the spectra were analyzed using fits for relative abundances from Weisman et al.[51] Figure 5 shows the relative percentage enrichment of the dissolved SWCNTs, grouped over four different diameter regimes, as a function of salt charge stoichiometries. The PL spectra were fitted for all species present in the samples and quantified as a percentage change in PL intensity compared to the as-received SWCNT $(n, m)$ population. SWCNT species with similar diameters showed similar trends as the charge stoichiometry changed. The $(NaC_{100})_{DIS}$ dissolved fraction showed an enrichment of the largest diameter sc-SWCNTs (>10 Å) with a similar enhancement of the second largest set (9.0−10 Å) albeit to a lesser magnitude. Conversely, the smallest SWCNTs in the distribution (<8.3 Å) showed the largest decrease with the second smallest set (8.3−9.0 Å) showing a smaller decrease in population. The most abundant SWCNT species changed from the $(7, 6)$ in the raw material to the larger $(11, 1)$ nanotube, demonstrating preferential dissolution of the larger diameter sc-SWCNTs at low charge added. As the charge on the salt is increased, for all other stoichiometries the most abundant species reverts to the $(7, 6)$, and relative abundances tend toward that of the starting $(n, m)$ distribution, due to the
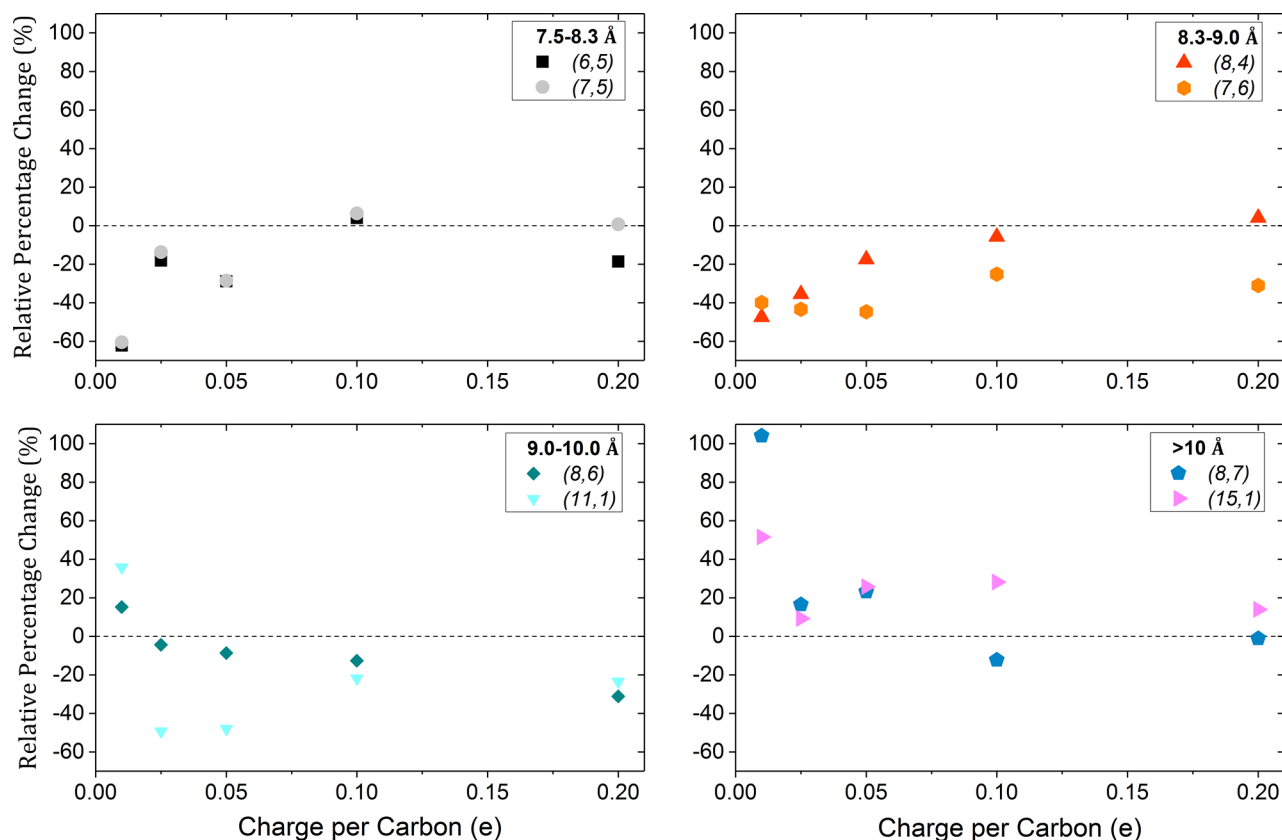


**Figure 5.** PL relative percentage change of the dissolved fractions for the eight most abundant SWCNTs in the HiPco raw batch R2-172, separated into four diameter regimes. The $NaC_{100}$ dissolved shows an enhancement of the larger diameter and a decrease of the smaller diameter sc-SWCNTs. Further charge moves the diameter distribution back toward that of the starting material.

successive dissolution of the smaller diameter sc-SWCNTs. This analysis is consistent with the measured increase in yield of dissolution. Furthermore, the change in the PL abundance of the (7, 6) SWCNT corroborates the Raman data, which showed the increase of the (7, 6) sc-SWCNT RBM with increasing charge.

Importantly, diameter selectivity as determined by PL shows excellent agreement with that determined from UV−vis−NIR as shown in Figure S5. This corroboration gives confidence in the analysis technique and validates the method for background subtraction for the UV−vis−NIR spectra.

The average diameter of the sc-SWCNTs from the as-produced powder was found to be 9.32 Å. The average diameters for each fraction were calculated from the PL data and are shown in Figure 6. The average sc-SWCNT diameter is
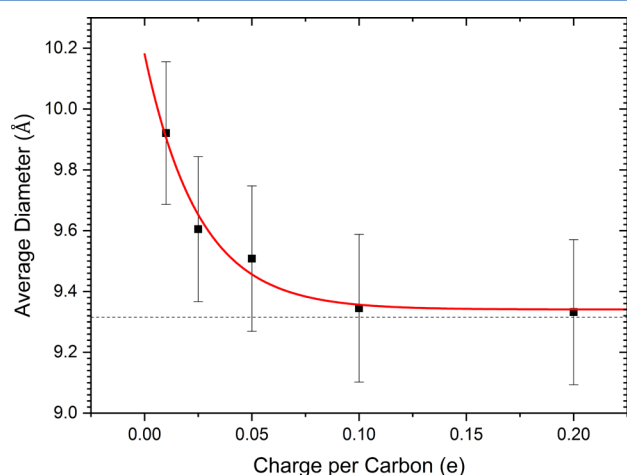


**Figure 6.** Mean SWCNT diameter and standard error of the various dissolved fractions as a function of charge, showing that the average diameter increases from that of the raw material as the charge level is decreased. The black dotted line represents the mean of the raw SWCNT sample population, and the red line is a guide for the eye.

largest for the $(NaC_{100})_{DIS}$ and decreases monotonically as the charge increases. For the two salts with the highest yields of dissolution, $NaC_{10}$ and $NaC_5$, the diameter distribution is the same within error as the starting material.

**3.5. e-DOS Analysis: Preferential Charging of Different SWCNT Species.** To understand the measured selective dissolution of different SWCNTs, a combined electronic density of states (e-DOS) was produced from extended tight binding models[52,53] summed over the SWCNT species present in the starting material. The e-DOS for the individual sc-SWCNTs were scaled according to their relative abundances, as experimentally determined by PL, and again by 73.8% for the overall proportion of sc-SWCNTs determined by the UV−vis−NIR absorption. The m-SWCNTs were scaled to 26.2% of the overall distribution, with each $(n, m)$ index within the diameter range determined by the PL given an equal weighting. The combined density of states is shown in Figure 7a. By integrating this function, the number of charges per carbon on a SWCNT as a function of chemical potential can be extracted separately for m-SWCNTs, small diameter (<9.0 Å) and larger diameter (>9.0 Å) sc-SWCNTs, shown in Figure 7b and compared to the enrichment measured in the spontaneously dissolve fractions as a function of charge.

The nominal charge stoichiometries for $NaC_{100}$ and $NaC_5$ are marked in Figure 7b, neglecting effects due to quantum
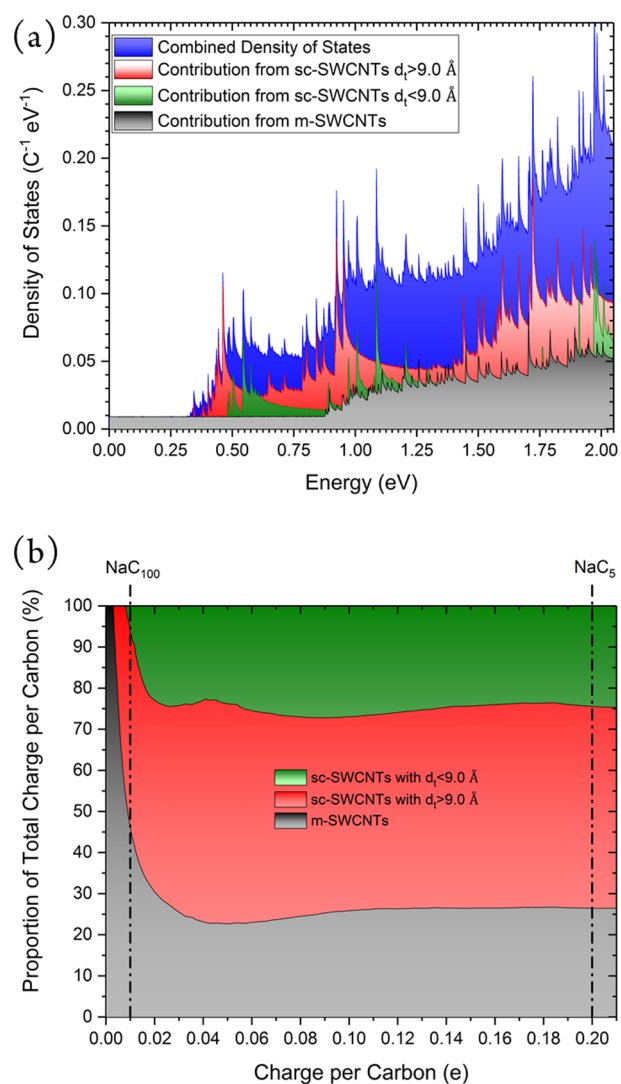


**Figure 7.** (a) Combined electronic density of states (1D e-DOS) for the HiPco R2−172 batch, derived empirically from PL and UV−vis−NIR data, separated into three components (small-diameter sc-SWCNT, large-diameter sc-SWCNT, and m-SWCNT). (b) Integrated DOS to give the proportion of electronic states per carbon for the individual components (small sc-SWCNT, large sc-SWCNT, and m-SWCNT) for a given stoichiometry of the total HiPco system.

capacitance[54] and charge lost to the amorphous carbon (which would cause a shift of the stoichiometries to lower charge per carbon values). For the $NaC_{100}$ salt, nearly half of the occupied electronic states are from m-SWCNTs. This indicates that at this charge ratio, m-SWCNTs will be reduced in preference to sc-SWCNTs as they have the most accessible states directly above the Fermi level. As uncharged SWCNTs are insoluble, the selective dissolution of the m-SWCNTs from the $NaC_{100}$ salt can be attributed to preferential charging of these species. However, above a Na:C ratio of about $NaC_{40}$, the proportion of electronic states that are attributed to m-SWCNTs remains relatively constant. This effect explains the lack of metallic enrichment at higher charge ratios observed from UV−vis−NIR (in Table 1). A similar argument can be made for the larger diameter sc-SWCNTs. As Figure 7b shows, aside from a small contribution from the smaller sc-SWCNTs for the $NaC_{100}$ stoichiometry, the rest of the occupied states arise from larger diameter sc-SWCNTs. The larger diameter sc-SWCNTs have

states closer to the Fermi level and will charge preferentially compared to smaller sc-SWCNTs, but after most m-SWCNTs. However, when the charge added is further increased, the smaller diameter SWCNTs will also be charged, and the diameter distribution returns to that of the starting material as measured in Figure 6.

**3.6. Cation Distribution.** To further investigate the mechanism behind the selective dissolution, the distribution of charge between the dissolved and undissolved SWCNTs was determined. To do this, the metal to carbon ratio for the dissolved and undissolved fractions of the same salt was measured using elemental analysis via inductively coupled plasma atomic emission spectroscopy (ICP-AES). Since a larger sample mass was needed, three selected nanotubides salts $NaC_5$, $NaC_{10}$, and $NaC_{30}$ were prepared from a new batch of HiPco SWCNTs, R1-821, and dissolved in DMF as before. In this batch, mass filtration measurements (see Figure S6) determined the yields of dissolution to be 54.8%, 89.1%, and 60.7% respectively, showing an even more pronounced reduction in yield of dissolution at higher charging than before (Figure 1). The difference in yield of dissolution between this batch and the previous one is due to the different amorphous carbon content, with the $I_{G_+}/I_D$ ratio larger in the newer batch (see Figure S7). The solutions were separated into dissolved and undissolved fractions before elemental analysis, and PL was performed (see Experimental Details).

Table 2 shows the measured sodium content of the fractions as a function of SWCNT diameter. For the $NaC_{30}$ salt, the

**Table 2. Stoichiometry of the Dissolved and Undissolved Fractions for an $NaC_5$ and an $NaC_{30}$ Salt, with the Corresponding Average Diameter for the Dissolved Fraction Compared to the As-Received Batch**

|  | salt | dissolved | undissolved |
|---|---|---|---|
| measured stoichiometry | $NaC_5$ | $NaC_{23.2}$ | $NaC_{1.5}$ |
| average sc-SWCNT diameter (Å) | 9.40 | 9.25 | 9.74 |
| measured stoichiometry | $NaC_{30}$ | $NaC_{20.0}$ | $NaC_{42.2}$ |
| average sc-SWCNT diameter (Å) | 9.40 | 9.61 | 9.36 |

system is in the regime below the maximum dissolution yield and the average diameter is, as expected, higher in the dissolved fraction. The dissolved fraction has a measured Na:C ratio of 1:20.0, compared to the undissolved 1:42.2. The differing values confirm the hypothesis that the larger SWCNTs, in the dissolved fraction, are preferentially charged. For $NaC_5$, we find a smaller average sc-SWCNT diameter and smaller dissolution yield in the dissolved fraction, as before. Interestingly, the dissolved fraction has a similar Na:C ratio of 1:23.2 as the Na:C ratio for the dissolved fraction of the $NaC_{30}$ salt. However, in the corresponding undissolved fraction, we now find significantly more sodium with a ratio of 1:1.5. This important finding clearly demonstrates that at very high charging the SWCNTs are not soluble, explaining the decrease in yield of dissolution. Moreover, this time it is the *largest* SWCNTs that do not dissolve. This result indicates that the metallic and large-diameter SWCNTs continue to be doped preferentially, but although first to be solubilized, eventually these tubes become too highly charged to dissolve.

This observation can be understood by considering the thermodynamics of the dissolution process. An ionic salt (such as sodium nanotubide) will dissolve if the free energy associated with the solvent-coordinated species is less than that of the combined free energy of the isolated ionic salt and solvent. The free energy of the salt will be largely dominated by its lattice enthalpy, as the magnitude of the entropic term will be small for an ordered crystal. In turn, the lattice enthalpy will be dependent on the ionic species involved; in general, the greater the charge density of the ions, the greater the magnitude of the lattice enthalpy.[55] This trend has been shown, for charged $C_{60}$ (fulleride) solutions, via Monte Carlo computer simulations studying the dissolution of fulleride salts as a function of charge.[14,56,57] In the case where the $C_{60}$ molecules are highly charged, the lattice enthalpy term is so great that there is no favorable gain of free energy upon solvation and thus they are not soluble. Similarly, here the SWCNTs that charge preferentially dissolve first but are the first to become too charged to dissolve at high levels of reduction, resulting in solutions of smaller diameter SWCNTs.

## 4. CONCLUSIONS

In summary, the selective dissolution of SWCNTs has been carefully investigated as a function of charge added to the as-produced SWCNT mix. From low to high charge, the selective dissolution trajectory is seen to favor first the amorphous carbon and defective material, followed by the m-SWCNTs, large-diameter sc-SWCNTs, and finally smaller diameter sc-SWCNTs, with an optimum charging value to give a maximized dissolution yield. The complex dissolution dependence on charging arises from the range of electronic structures of the SWCNT species in the sample. At low doping, the SWCNTs with the states available closest to the Fermi level are preferentially charged and therefore preferentially dissolve. At higher metal loadings, the excess charge on the large-diameter SWCNTs prevents their dissolution, as confirmed by the observation of charge partitioning between dissolved and undissolved fractions.

The analysis of the enriched fractions clearly shows that reliance on Raman spectroscopy to determine separation can be misleading, and a valid picture necessitates a range of complementary methods including UV−vis−NIR and PL. The trajectory of nanotube dissolution also demonstrates that SWCNTs within a mixed sample can themselves be viewed as discrete molecular species, with the equilibrium charge distribution that results upon fixed doping being governed by the differing electron affinities of the SWCNTs. The results also highlight the importance of the balance of the thermodynamics of the dissolution process, in particular demonstrating that for very highly charged SWCNTs dissolution is unfavorable. This conclusion will be an important consideration for controlling concentrations and dissolution via alkali-metal reduction not just for SWCNTs[58] but also graphene[33,59,60] and other 2d-materials.[15]

## ■ ASSOCIATED CONTENT

**ⓢ Supporting Information**

The Supporting Information is available free of charge on the ACS Publications website at DOI: 10.1021/acs.jpcc.7b06553.

Calculation of the extinction coefficient as a function of charge on the nanotubes (Figure S1); Raman Spectroscopy of the SEM sample shown in Figure 2e, f (Figure S2); UV−vis−NIR spectra of the dissolved SWCNT solutions after aqueous redispersion and corresponding discussion (Figure S3); photoluminescence (PL) analysis showing the opposite trends in the undissolved and

Article

dissolved SWCNTs for two different stoichiometries (Figure S4); comparison of the diameter enrichment for UV−vis−NIR and PL (Figure S5); yield of dissolution measurements for the newer batch as a function of stoichiometry (Figure S6); Raman spectroscopy comparison of the two batches used in this study (Figure S7); explanation of the calculation for Figure 7b (Figure S8) (PDF)

## ■ AUTHOR INFORMATION

### Notes

The authors declare no competing financial interest.

## ■ ABBREVIATIONS

DMF, *N*,*N*-dimethylformamide
DOC, sodium deoxycholate
e-DOS, electronic density of states
ICP-AES, inductively coupled plasma atomic emission spectroscopy
m-, metallic
PL, photoluminescence
RBM, radial breathing mode
sc-, semiconducting
SEM, scanning electron microscopy
TGA, thermogravimetric analysis
UV−vis−NIR, ultraviolet−visible−near-infrared

## ■ REFERENCES

(1) Liu, C.; Cheng, H.-M. Controlled growth of semiconducting and metallic single-wall carbon nanotubes. *J. Am. Chem. Soc.* **2016**, *138*, 6690−6698.

(2) Yang, F.; Wang, X.; Zhang, D.; Yang, J.; Luo, D.; Xu, Z.; Wei, J.; Wang, J.-Q.; Xu, Z.; Peng, F.; et al. Chirality-specific growth of single-walled carbon nanotubes on solid alloy catalysts. *Nature* **2014**, *510*, 522−524.

(3) Yao, Y.; Feng, C.; Zhang, J.; Liu, Z. Cloning" of single-walled carbon nanotubes via open-end growth mechanism. *Nano Lett.* **2009**, *9*, 1673−1677.

(4) Jorio, A.; Santos, A. P.; Ribeiro, H. B.; Fantini, C.; Souza, M.; Vieira, J. P. M.; Furtado, C. A.; Jiang, J.; Saito, R.; Balzano, L.; Resasco, D. E.; Pimenta, M. A.; et al. Quantifying carbon-nanotube species with resonance Raman scattering. *Phys. Rev. B: Condens. Matter Mater. Phys.* **2005**, *72*, 075207.

(5) Hu, H.; Zhao, B.; Itkis, M. E.; Haddon, R. C. Nitric acid purification of single-walled carbon nanotubes. *J. Phys. Chem. B* **2003**, *107*, 13838−13842.

(6) Wang, Y. H.; Shan, H. W.; Hauge, R. H.; Pasquali, M.; Smalley, R. E. A highly selective, one-pot purification method for single-walled carbon nanotubes. *J. Phys. Chem. B* **2007**, *111*, 1249−1252.

(7) Monthioux, M.; Smith, B.; Burteaux, B.; Claye, A.; Fischer, J.; Luzzi, D. Sensitivity of single-wall carbon nanotubes to chemical processing: an electron microscopy investigation. *Carbon* **2001**, *39*, 1251−1272.

(8) Liu, H.; Nishide, D.; Tanaka, T.; Kataura, H. Large-scale single-chirality separation of single-wall carbon nanotubes by simple gel chromatography. *Nat. Commun.* **2011**, *2*, 309.

(9) Green, A. A.; Hersam, M. C. Nearly single-chirality single-walled carbon nanotubes produced via orthogonal iterative density gradient ultracentrifugation. *Adv. Mater.* **2011**, *23*, 2185−2190.

(10) Lucas, A.; Zakri, C.; Maugey, M.; Pasquali, M.; Schoot, P. v. d.; Poulin, P. Kinetics of nanotube and microfiber scission under sonication. *J. Phys. Chem. C* **2009**, *113*, 20599−20605.

(11) Coleman, J. N. Liquid-phase exfoliation of nanotubes and graphene. *Adv. Funct. Mater.* **2009**, *19*, 3680−3695.

(12) Pénicaud, A.; Poulin, P.; Derré, A.; Anglaret, E.; Petit, P. Spontaneous dissolution of a single-wall carbon nanotube salt. *J. Am. Chem. Soc.* **2005**, *127*, 8−9.

(13) Fogden, S.; Howard, C. A.; Heenan, R. K.; Skipper, N. T.; Shaffer, M. S. P. Scalable method for the reductive dissolution, purification, and separation of single-walled carbon nanotubes. *ACS Nano* **2012**, *6*, 54−62.

(14) Howard, C. A.; Wasse, J. C.; Skipper, N. T.; Thompson, H.; Soper, A. K. The solvation structure of fulleride $C_{60}^{5-}$ anions in potassium ammonia solution. *J. Phys. Chem. C* **2007**, *111*, 5640−5647.

(15) Cullen, P. L.; Cox, K. M.; Bin Subhan, M. K.; Picco, L.; Payton, O. D.; Buckley, D. J.; Miller, T. S.; Hodge, S. A.; Skipper, N. T.; Tileli, V.; Howard, C. A.; et al. Ionic solutions of two-dimensional materials. *Nat. Chem.* **2017**, *9*, 244−249.

(16) Hodge, S. A.; Fogden, S.; Howard, C. A.; Skipper, N. T.; Shaffer, M. S. P. Electrochemical processing of discrete single-walled carbon nanotube anions. *ACS Nano* **2013**, *7*, 1769−1778.

(17) Jiang, C.; Saha, A.; Marti, A. A. Carbon nanotubides: an alternative for dispersion, functionalization and composites fabrication. *Nanoscale* **2015**, *7*, 15037−15045.

(18) Gebhardt, J.; Bosch, S.; Hof, F.; Hauke, F.; Hirsch, A.; Görling, A. Selective reduction of SWCNTs—Concepts and insights. *J. Mater. Chem. C* **2017**, *5*, 3937−3947.

(19) Wunderlich, D.; Hauke, F.; Hirsch, A. Preferred functionalization of metallic and small-diameter single walled carbon nanotubes via reductive alkylation. *J. Mater. Chem.* **2008**, *18*, 1493−1497.

(20) Voiry, D.; Drummond, C.; Pénicaud, A. Portrait of carbon nanotube salts as soluble polyelectrolytes. *Soft Matter* **2011**, *7*, 7998−8001.

(21) O'Connell, M. J.; Sivaram, S.; Doorn, S. K. Near-infrared resonance Raman excitation profile studies of single-walled carbon nanotube intertube interactions: A direct comparison of bundled and individually dispersed HiPco nanotubes. *Phys. Rev. B: Condens. Matter Mater. Phys.* **2004**, *69*, 235415.

(22) Araujo, P. T.; Fantini, C.; Lucchese, M. M.; Dresselhaus, M. S.; Jorio, A. The effect of environment on the radial breathing mode of supergrowth single wall carbon nanotubes. *Appl. Phys. Lett.* **2009**, *95*, 261902.

(23) Filho, A. G. S.; Jorio, A.; Samsonidze, G. G.; Dresselhaus, G.; Saito, R.; Dresselhaus, M. S. Raman spectroscopy for probing chemically/physically induced phenomena in carbon nanotubes. *Nanotechnology* **2003**, *14*, 1130.

(24) Müller, M.; Maultzsch, J.; Wunderlich, D.; Hirsch, A.; Thomsen, C. Raman spectroscopy on chemically functionalized carbon nanotubes. *Phys. Status Solidi B* **2007**, *244*, 4056−4059.

(25) Hennrich, F.; Krupke, R.; Lebedkin, S.; Arnold, K.; Fischer, R.; Resasco, D. E.; Kappes, M. M. Raman spectroscopy of individual single-walled carbon nanotubes from various sources. *J. Phys. Chem. B* **2005**, *109*, 10567−10573.

(26) Gebhardt, B.; Syrgiannis, Z.; Backes, C.; Graupner, R.; Hauke, F.; Hirsch, A. Carbon nanotube sidewall functionalization with carbonyl compounds—modified Birch conditions vs the organometallic reduction approach. *J. Am. Chem. Soc.* **2011**, *133*, 7985−7995.

(27) Arepalli, S.; Freiman, S. W.; Hooker, S. A.; Migler, K. D. *Measurement issues in single-wall carbon nanotubes*; National Institute of Standards and Technology Special Publication (NIST-SP), 2008, 960.19.

(28) Chen, F.; Xue, Y.; Hadjiev, V. G.; Chu, C.; Nikolaev, P.; Arepalli, S. Fast characterization of magnetic impurities in single-walled carbon nanotubes. *Appl. Phys. Lett.* **2003**, *83*, 4601−4603.

(29) O'Connell, M. J.; Eibergen, E. E.; Doorn, S. K. Chiral selectivity in the charge-transfer bleaching of single-walled carbon-nanotube spectra. *Nat. Mater.* **2005**, *4*, 412−418.

(30) Clancy, A. J.; Melbourne, J.; Shaffer, M. S. P. A one-step route to solubilised, purified or functionalised single-walled carbon nanotubes. *J. Mater. Chem. A* **2015**, *3*, 16708−16715.

(31) Dresselhaus, M. S.; Jorio, A.; Souza Filho, A. G.; Saito, R. Defect characterization in graphene and carbon nanotubes using Raman spectroscopy. *Philos. Trans. R. Soc., A* **2010**, *368*, 5355−5377.

(32) Maultzsch, J.; Telg, H.; Reich, S.; Thomsen, C. Radial breathing mode of single-walled carbon nanotubes: Optical transition energies and chiral-index assignment. *Phys. Rev. B: Condens. Matter Mater. Phys.* **2005**, *72*, 205438.

(33) Catheline, A.; Vallés, C.; Drummond, C.; Ortolani, L.; Morandi, V.; Marcaccio, M.; Iurlo, M.; Paolucci, F.; Pénicaud, A. Graphene solutions. *Chem. Commun.* **2011**, *47*, 5470−5472.

(34) Pénicaud, A.; Valat, L.; Derré, A.; Poulin, P.; Zakri, C.; Roubeau, O.; Maugey, M.; Miaudet, P.; Anglaret, E.; Petit, P.; et al. Mild dissolution of carbon nanotubes: composite carbon nanotube fibres from polyelectrolyte solutions. *Compos. Sci. Technol.* **2007**, *67*, 795−797.

(35) Hodge, S. A.; Buckley, D. J.; Yau, H. C.; Skipper, N. T.; Howard, C. A.; Shaffer, M. S. P. Chemical routes to discharging graphenides. *Nanoscale* **2017**, *9*, 3150−3158.

(36) Chiang, I. W.; Brinson, B. E.; Huang, A. Y.; Willis, P. A.; Bronikowski, M. J.; Margrave, J. L.; Smalley, R. E.; Hauge, R. H. Purification and characterization of single-wall carbon nanotubes (SWNTs) obtained from the gas-phase decomposition of CO (HiPco Process). *J. Phys. Chem. B* **2001**, *105*, 8297−8301.

(37) Bachilo, S. M.; Strano, M. S.; Kittrell, C.; Hauge, R. H.; Smalley, R. E.; Weisman, R. B. Structure-assigned optical spectra of single-walled carbon nanotubes. *Science* **2002**, *298*, 2361−2366.

(38) Jorio, A.; Souza Filho, A. G.; Dresselhaus, G.; Dresselhaus, M. S.; Swan, A. K.; Ünlü, M. S.; Goldberg, B. B.; Pimenta, M. A.; Hafner, J. H.; Lieber, C. M.; Saito, R.; et al. G-band resonant Raman study of 62 isolated single-wall carbon nanotubes. *Phys. Rev. B: Condens. Matter Mater. Phys.* **2002**, *65*, 155412.

(39) Brown, S. D. M.; Jorio, A.; Corio, P.; Dresselhaus, M. S.; Dresselhaus, G.; Saito, R.; Kneipp, K. Origin of the Breit−Wigner−Fano lineshape of the tangential G-band feature of metallic carbon nanotubes. *Phys. Rev. B: Condens. Matter Mater. Phys.* **2001**, *63*, 155414.

(40) Qiu, H.; Maeda, Y.; Akasaka, T. Facile and scalable route for highly efficient enrichment of semiconducting single-walled carbon nanotubes. *J. Am. Chem. Soc.* **2009**, *131*, 16529−16533.

(41) O'Connell, M. J.; Bachilo, S. M.; Huffman, C. B.; Moore, V. C.; Strano, M. S.; Haroz, E. H.; Rialon, K. L.; Boul, P. J.; Noon, W. H.; Kittrell, C.; et al. Band gap fluorescence from individual single-walled carbon nanotubes. *Science* **2002**, *297*, 593−596.

(42) Liu, H.; Tanaka, T.; Feng, Y.; Kataura, H. Diameter-selective desorption of semiconducting single-wall carbon nanotubes from agarose gel. *Phys. Status Solidi B* **2010**, *247*, 2649−2652.

(43) Paolucci, D.; Franco, M. M.; Iurlo, M.; Marcaccio, M.; Prato, M.; Zerbetto, F.; Pénicaud, A.; Paolucci, F. Singling out the electrochemistry of individual single-walled carbon nanotubes in solution. *J. Am. Chem. Soc.* **2008**, *130*, 7393−7399.

(44) Naumov, A. V.; Ghosh, S.; Tsyboulski, D. A.; Bachilo, S. M.; Weisman, R. B. Analyzing absorption backgrounds in single-walled carbon nanotube spectra. *ACS Nano* **2011**, *5*, 1639−1648.

(45) Nair, N.; Usrey, M. L.; Kim, W.-J.; Braatz, R. D.; Strano, M. S. Estimation of the (n,m) concentration distribution of single-walled carbon nanotubes from photoabsorption spectra. *Anal. Chem.* **2006**, *78*, 7689−7696.

(46) *Characterization of single-wall carbon nanotubes using ultraviolet−visible−near infrared (UV−Vis−NIR) absorption spectroscopy*; The International Organization for Standardization, DD ISO/TS 10868:2017, 2017.

(47) Huang, H.; Kajiura, H.; Maruyama, R.; Kadono, K.; Noda, K. Relative optical absorption of metallic and semiconducting single-walled carbon nanotubes. *J. Phys. Chem. B* **2006**, *110*, 4686−4690.

(48) Paredes, J. I.; Burghard, M. Dispersions of individual single-walled carbon nanotubes of high length. *Langmuir* **2004**, *20*, 5149−5152.

(49) Kuwahara, S.; Kuwahara, Y.; Shinohara, H. Quantitative analysis of isolated single-wall carbon nanotubes with their molar absorbance coefficients. *J. Nanomater.* **2014**, *2014*, 262940.

(50) Weisman, R. B.; Bachilo, S. M. Dependence of optical transition energies on structure for single-walled carbon nanotubes in aqueous suspension: an empirical Kataura plot. *Nano Lett.* **2003**, *3*, 1235−1238.

(51) Tsyboulski, D. A.; Rocha, J.-D. R.; Bachilo, S. M.; Cognet, L.; Weisman, R. B. Structure-dependent fluorescence efficiencies of individual single-walled carbon nanotubes. *Nano Lett.* **2007**, *7*, 3080−3085.

(52) Sato, K.; Saito, R.; Jiang, J.; Dresselhaus, G.; Dresselhaus, M. S. Discontinuity in the family pattern of single-wall carbon nanotubes. *Phys. Rev. B: Condens. Matter Mater. Phys.* **2007**, *76*, 195446.

(53) Nugraha, A. R. T.; Saito, R.; Sato, K.; Araujo, P. T.; Jorio, A.; Dresselhaus, M. S. Dielectric constant model for environmental effects on the exciton energies of single wall carbon nanotubes. *Appl. Phys. Lett.* **2010**, *97*, 091905.

(54) Hodge, S. A.; Tay, H. H.; Anthony, D. B.; Menzel, R.; Buckley, D. J.; Cullen, P. L.; Skipper, N. T.; Howard, C. A.; Shaffer, M. S. P. Probing the charging mechanisms of carbon nanomaterial polyelectrolytes. *Faraday Discuss.* **2014**, *172*, 311−325.

(55) Murrell, J. N.; Jenkins, A. D. *Properties of liquids and solutions*; Wiley & Sons, Chichester, U.K., 1994.

(56) Howard, C. A.; Skipper, N. T. Computer simulations of fulleride anions in metal−ammonia solutions. *J. Phys. Chem. B* **2009**, *113*, 3324−3332.

(57) Howard, C. A.; Thompson, H.; Wasse, J. C.; Skipper, N. T. Formation of giant solvation shells around fulleride anions in liquid ammonia. *J. Am. Chem. Soc.* **2004**, *126*, 13228−13229.

(58) Clancy, A. J.; Anthony, D. B.; Fisher, S. J.; Leese, H. S.; Roberts, C. S.; Shaffer, M. S. P. Reductive dissolution of supergrowth carbon nanotubes for tougher nanocomposites by reactive coagulation spinning. *Nanoscale* **2017**, *9*, 8764−8773.

(59) Milner, E. M.; Skipper, N. T.; Howard, C. A.; Shaffer, M. S. P.; Buckley, D. J.; Rahnejat, K. A.; Cullen, P. L.; Heenan, R. K.; Lindner, P.; Schweins, R. Structure and morphology of charged graphene platelets in solution by small-angle neutron scattering. *J. Am. Chem. Soc.* **2012**, *134*, 8302−8305.

(60) Vallés, C.; Drummond, C.; Saadaoui, H.; Furtado, C. A.; He, M.; Roubeau, O.; Ortolani, L.; Monthioux, M.; Pénicaud, A. Solutions of negatively charged graphene sheets and ribbons. *J. Am. Chem. Soc.* **2008**, *130*, 15802−15804.